An array based seismic image on the Dahutang deposit, South China: Insight into the mineralization

Zhou Zhang [a,b], Yangfan Deng [a,*], Junming Yao [c,d], Jianye Zong [a,b,e], Huayong Chen [d]

[a] State Key Laboratory of Isotope Geochemistry, Guangzhou Institute of Geochemistry, Chinese Academy of Sciences, Guangzhou, China
[b] College of Earth and Planetary Sciences, University of Chinese Academy of Sciences, Beijing, China
[c] Xinjiang Research Center for Mineral Resources, Xinjiang Institute of Ecology and Geography, Chinese Academy of Sciences, Urumqi, China
[d] Key Laboratory of Mineralogy and Metallogeny, Guangzhou Institute of Geochemistry, Chinese Academy of Sciences, Guangzhou, China
[e] International Research Center for Planetary Science, Chengdu University of Technology, Chengdu, China

ABSTRACT

As a world-class W–Cu–Mo polymetallic deposit in South China, there are lots of studies focusing on the geochemical characteristics and metallogeny in this region, however, geophysical observations with special attention on the deep structure of the ore district are quite few. In order to better understand the metallogenic mechanism at Dahutang region, we deployed a dense seismic array and then performed the seismic image to get the deep structure, including the ambient noise tomography, receiver function calculation, H-κ stacking and joint inversion of receiver function and surface wave dispersion. The Moho depth deepens from the south to the north along the array. The seismic image and gravity anomaly show a low velocity in the upper crust, high velocity in the middle-lower crust, relatively high Vp/Vs ratio, and low gravity anomaly beneath the Dahutang deposit. These features may indicate the process of mineralization: under the context of lithospheric extension and thinning in the Late Mesozoic, there are some magma underplating and melting the lower crust. The hot melts migrated upward and differentiated, the dense component cooled in the middle-lower crust to form the high velocity zones. The light component intruded into the Neoproterozoic granite and formed the Mesozoic granite, providing the heat and material source for the further enrichment of tungsten-copper polymetallic ore.

1. Introduction

The Dahutang deposit is a newly discovered giant W-Cu-Mo deposit, which is located in the central part of the Jiangnan Orogen, South China (Fig. 1a). As one of largest WO^3 deposits in the world, Dahutang is recently reported to store an estimated resource of 1.1 million tons (Mt) of WO^3 (Song et al., 2018a). Due to its economic and geological significance, the genesis mechanism of the deposit attracts great attention.

It is well accepted that this deposit is related with the magmatism in Yanshanian movement (Jiang et al., 2015; Han et al., 2016; Ye et al., 2016; Song et al., 2018a; Sun et al., 2012; Yang and Sun, 2018). During this period, there are widely distributed granites in South China (Zhou et al., 2006). Ye et al. (2016) believed that the rock and ore-forming processes at Dahutang deposit are under a geodynamic setting of lithospheric thinning and extension based on the U—Pb Geochronology. The biotite granite porphyry of early Cretaceous is also reported from lithospheric extension and mantle upwelling due to the subduction of

Paleo-Pacific plate subduction into South China (Chu et al., 2019). This process is consistent with the large-scale tungsten-tin polymetallic mineralization in the Qinhang metallogenic belt (~2000 km length, 70–30 km in width), South China (Mao et al., 2011). Fluid intrusion and oxygen fugacity are widely accepted as two important factors to affect the final mineralization in Dahutang according to the geochemical analysis (Han et al., 2016; Ye et al., 2016; Yao et al., 2016; Song et al., 2018b; Cao et al., 2020). Combined with previous geochronological studies on magmatism and mineralization (Feng et al., 2012; Xiang et al., 2012; Huang and Jiang, 2012, 2013, 2014; Mao et al., 2013, 2015; Xiang et al., 2013a, 2013b; Jiang et al., 2015; Ye et al., 2016; Zhang et al., 2016; Zhang et al., 2018b), the recent study showed that the multiphase magmatism and continuous accumulation of mineralization for a long period of time (151–130 Ma) have contributed to the formation of the giant Dahutang deposit (Song et al., 2018a). However, the deep structure of Dahutang deposit is still unknown, and the reason for such a rare 20 m.y. long-lived multiphase magmatism and successive
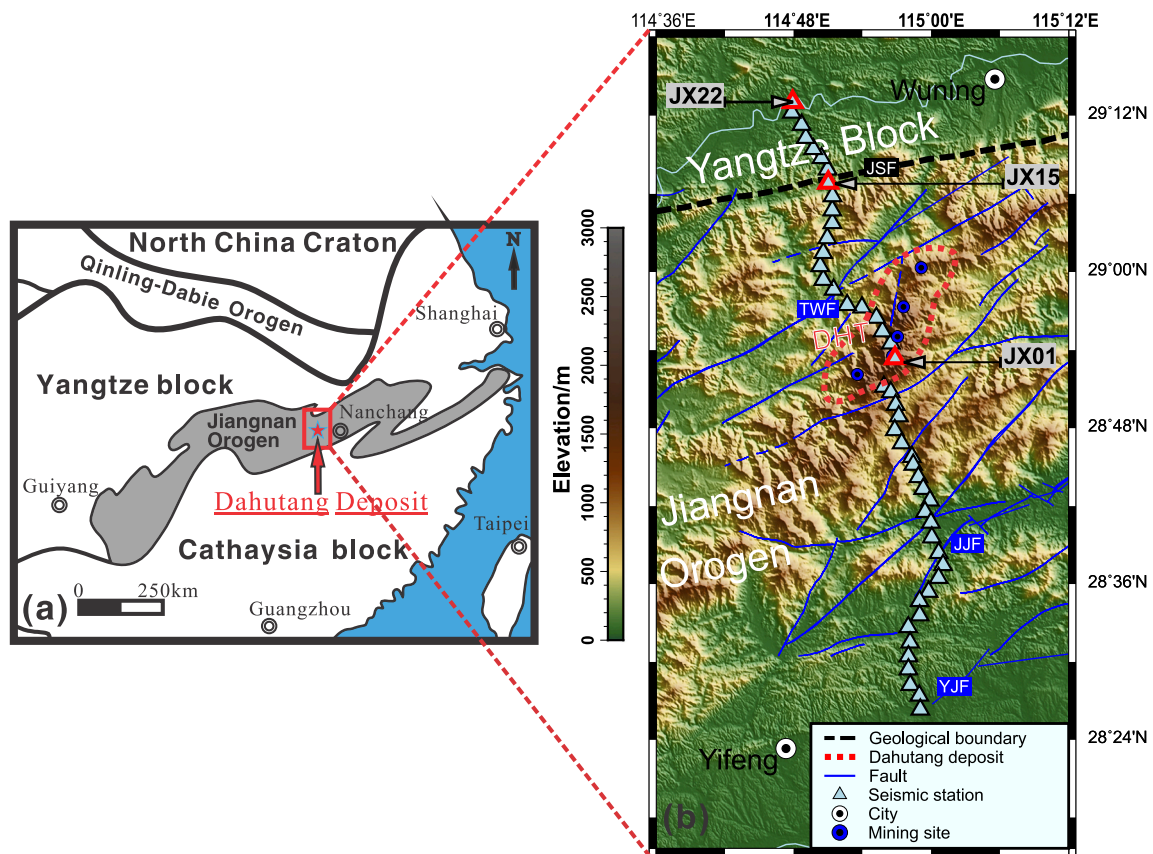
Fig. 1. (a) Location and regional geologic sketch of our study area (modified after Zhang et al., 2018b). The main geological regions in South China and the adjacent areas are shown, including the North China Craton, Qinling-Dabie Orogen, Yangtze block, Jiangnan Orogen and Cathaysia block. The red box marks our study region in a large area. (b) Geological background of our study region. The light-blue triangles with black line indicate the stations we deployed. The blue dots indicate the recent mining sites in Dahutang deposit. The blue lines indicate faults (based on Deng et al., 2003; Han et al., 2016). The black dashed line (marked JSF) indicates the geological boundary between Yangtze block and Jiangnan Orogen (Yao et al., 2013b). Station JX22 is marked for Fig. 3(b) while stations JX01 and JX15 are marked for Fig. 2. Abbreviations: DHT, Dahutang deposit; JSF, Jiujiang-Shitai fault; TWF, Tonggu-Wuning fault; JJF, Jiujiang-Jinan fault; YJF, Yifeng-Jingdezhen fault. (For interpretation of the references to colour in this figure legend, the reader is referred to the web version of this article.)

mineralization is puzzled.

There are several large scale geophysical investigations in South China, including active seismic profile (Deng et al., 2011), ambient noise tomography (Zhou et al., 2012), receiver function (He et al., 2013; Song et al., 2017), density inversion from gravity and seismic constraints (Deng et al., 2014), and joint inversion of receiver function and gravity anomaly (Guo et al., 2019), but they have low resolution at Dahutang district. Even Yao et al. (2013b) performed the gravity explosion on the distribution of intrusive rocks at shallow depth; there are no geophysical observations with special attention on the deep structure beneath Dahutang deposit.

In order to reveal the deep structure and better understand the mineralization in Dahutang region, we deployed a dense array cutting across the deposit. We first performed ambient noise tomography to get the shallow structure and then obtained the main interface and average crustal Vp/Vs from receiver function. Lastly, we used the joint inversion of receiver function and surface wave dispersion to get the whole crustal structure. The possible mechanism for the formation of the Dahutang deposit is proposed based on previous frameworks and our new result.

2. Geological background

The Dahutang deposit is located in the central part of Jiangnan orogen, which is believed to result from the collision between the Yangtze and Cathaysia blocks during the Neoproterozoic period (Li et al., 2001; Li et al., 2003; Zhou et al., 2006; Shu, 2012). Later on, this

region reactivated at the Mesozoic due to the Paleo-pacific subduction (Li et al., 2016). The granites outcrop in this region could be divided into two main periods, the Neoproterozoic granite and Yanshanian granite. The later one formed a large number of deposits in this area, including tungsten, copper and tin (Hua et al., 2003). The sedimentary rocks at Dahutang deposit include Neoproterozoic Shuangqiaoshan Group with metamorphosed turbiditic sandstone interbeds (Song et al., 2018b). The Neoproterozoic Jiuling biotite granodiorite is covered by Quaternary sediment and outcrop only in South Dahutang deposit. The faults in this region trend mainly in EW (or NEE) and NE-NNE directions, exhibiting good channels for the fluid intrusion. In particular, the Jiujiang-Shitai fault (JSF) divides the array into two principal geological units: the Yangtze block, and the Jiangnan Orogen (Yao et al., 2013a).

3. Data

We deployed a linear dense seismic array in Oct 2018, with the trend oriented in NW-SE direction that cut across the main geological units. Dahutang deposit is located in the center of the array where also the high topography (Fig. 1b) has. This array includes 50 three-component short-period portable seismographs (QS-05A, with 120 Hz-10 s bandwidth; marked by the light blue triangles in Fig. 1b), and the distance interval is ~2 km. We finally got the data from 47 stations, and the average duration of the seismic stations is 14 days. The detailed data information is shown in Table S1. The P wave receiver function and short period group dispersion were measured based on this data.
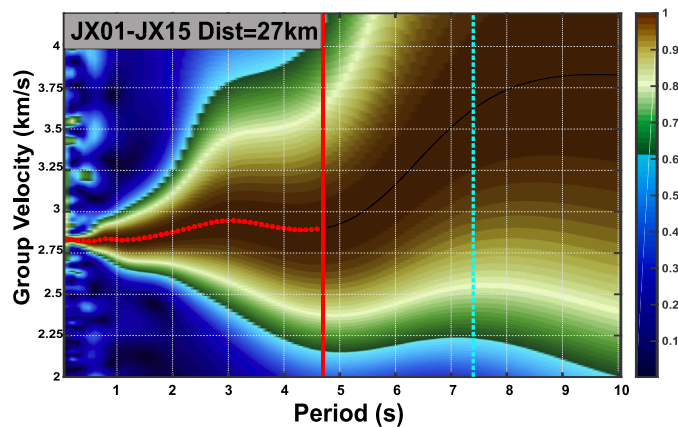
Fig. 2. An example of the analysis of Rayleigh wave group velocity dispersion curve. Horizontal axis is period (s). Vertical axis is the group velocity (km/s). Different colour shows normalized surface wave envelope amplitude at different velocity and period. Red solid line illustrates the station distance equals to two times wavelength while light blue dashed line represents that the station distance equals to one wavelength. The red dots are the final picked dispersions. (For interpretation of the references to colour in this figure legend, the reader is referred to the web version of this article.)

The long period dispersion data comes from an ambient noise tomography of China (Shen et al., 2016), which involves more than 2000 stations and the resolution of group velocity in South China is 50 km. In this study, according to an inverse-weighted-distance interpolation algorithm proposed by Deng et al. (2015), we extracted group dispersion curves from the dispersion maps of 8–50 s (Shen et al., 2016) at each station. Bouguer gravity anomaly along the array was sourced from the Earth Gravitational Model 2008 generated by Pavlis et al. (2012), which provides a $2.5' \times 2.5'$ sized grid including synthetic gravity generated by the terrestrial gravity anomaly and GRACE data.

4. Method

We follow the common data procedure developed by Bensen et al. (2007) to calculate cross-correlations. The detailed process includes the following steps, (1) Merge the data and decimate it to 0.02 s; (2) generate hourly vertical component SAC format data at each station; (3) remove the mean, trend, and instrument response, and filter the data with 0.1–10 s bandpass; (4) whiten and normalize the data; (5) calculate cross-correlation; (6) stack the noise cross-correlation functions (NCFs) at each station pair to obtain the NCFs. Finally, we manually picked the group velocity dispersion data in the period range of 0.1–10s using a Time-Frequency analysis method (Yao et al., 2006). Fig. 2 shows an example of extracting Rayleigh wave group velocity dispersion curve. Two quality control measures are applied to choose the good dispersion: we only keep the dispersion with interstation distance greater than 2 times of the surface-wave wavelength, to avoid unreliable measurements from short-distance station pairs; Dispersions are removed if the signal-to-noise ratio (SNR) is lower than 5. In addition, we visually remove some dispersion curves with weird high velocity (>4.0 km/s in the short period).

Fast Marching Surface Tomography (FMST) (Rawlinson et al., 2006) is applied to invert the mixed path Rayleigh wave group velocity. This program minimizes the differences between observed and calculated travel-times by updating the propagation paths. Due to its high efficiency and applicability, this method is widely used to do tomographic imaging and track multiple phases (Rawlinson and Sambridge, 2005). CPS330 program (Herrmann, 2013) gives a linear algorithm to do the S-wave velocity inversion. This program is well-known for its efficiency and stability, especially when dealing with the short period dispersions. Hence we employed the CPS330 program to get the shallow S wave velocity along our array based on the inverted group velocities.

P wave receiver-function image and H–κ stacking technique (Zhu and Kanamori, 2000) provide insightful tools to analyze discontinuities,

the latter one can further obtain crustal thickness (H) and Vp/Vs ratio (κ) simultaneously. To calculate the receiver functions, we selected teleseismic P waveforms from 102 earthquakes with magnitudes Mw ≥ 5 and epicentral distances ranging from 30° to 90° between 2018 and 10-09 and 2018-11-09 (Fig. 7a). A time-domain iterative deconvolution method (Ligorria and Ammon, 1999) with a Gaussian filter of 1.0 s (set α=2.5) was applied to obtain the receiver functions, and then the moveout correction (Yuan et al., 1997) was performed with reference slowness of 6.4 s/deg. based on the IASP91 model (Kennett and Engdahl, 1991). In order to eliminate poor receiver functions, we visually inspected all receiver functions and chose those with high signal-to-noise ratio. We then carried out the H–κ stacking (Zhu and Kanamori, 2000) to estimate the crustal thickness and Vp/Vs ratio at each station. During this calculation, an average Vp of 6.3 km/s was utilized, and the weight coefficients for the amplitudes of Ps, PpPs, and PsPs+PpSs were set to 0.6, 0.3, and 0.1, respectively. In addition, we searched the crust thickness from 20 to 60 km and Vp/Vs ratio from 1.5 to 2.0.

Joint inversion has been widely used to reduce the non-uniqueness and improve the reliability of geophysical inversion. As the P-wave receiver function is sensitive to impedance contrasts while the surface wave dispersion is sensitive to vertical shear-velocity averages, joint inversion of these two parameters can combine their advantages. We apply a joint inversion method developed by Li et al. (2017) to get the crustal S wave velocity, which employs the Neighborhood Algorithm (NA) for parametric search, including the Moho depth and sediment. Li et al. (2017) has made several synthetic tests to illustrate the robustness of the method, including different sedimentary thickness, Moho depth, crustal low-velocity zone, and crustal high-velocity zone. Ye et al. (2017) and Deng et al. (2018, 2019a, 2019b) have applied this method successfully in Northeast Tibet and South China to get reliable crustal Vs and Vp/Vs models. In this study, we prepare the dispersion by combining the short period dispersion from the deployed array with the long period (8–50s) dispersion from Shen et al. (2016) and prepare the receiver function by cutting the stacked P receiver functions within 15 s.

5. Results

5.1. Resolution validation

We finally picked 932 Rayleigh wave group velocity dispersion curves (Fig. 3a) based on the time-frequency analysis. Then we followed Bem et al. (2020) to do the "outlier removal" by removing the dispersions greater than 2.5 times the standard deviation from the average velocity (the black dashed line in Fig. 3a). The used dispersions (the
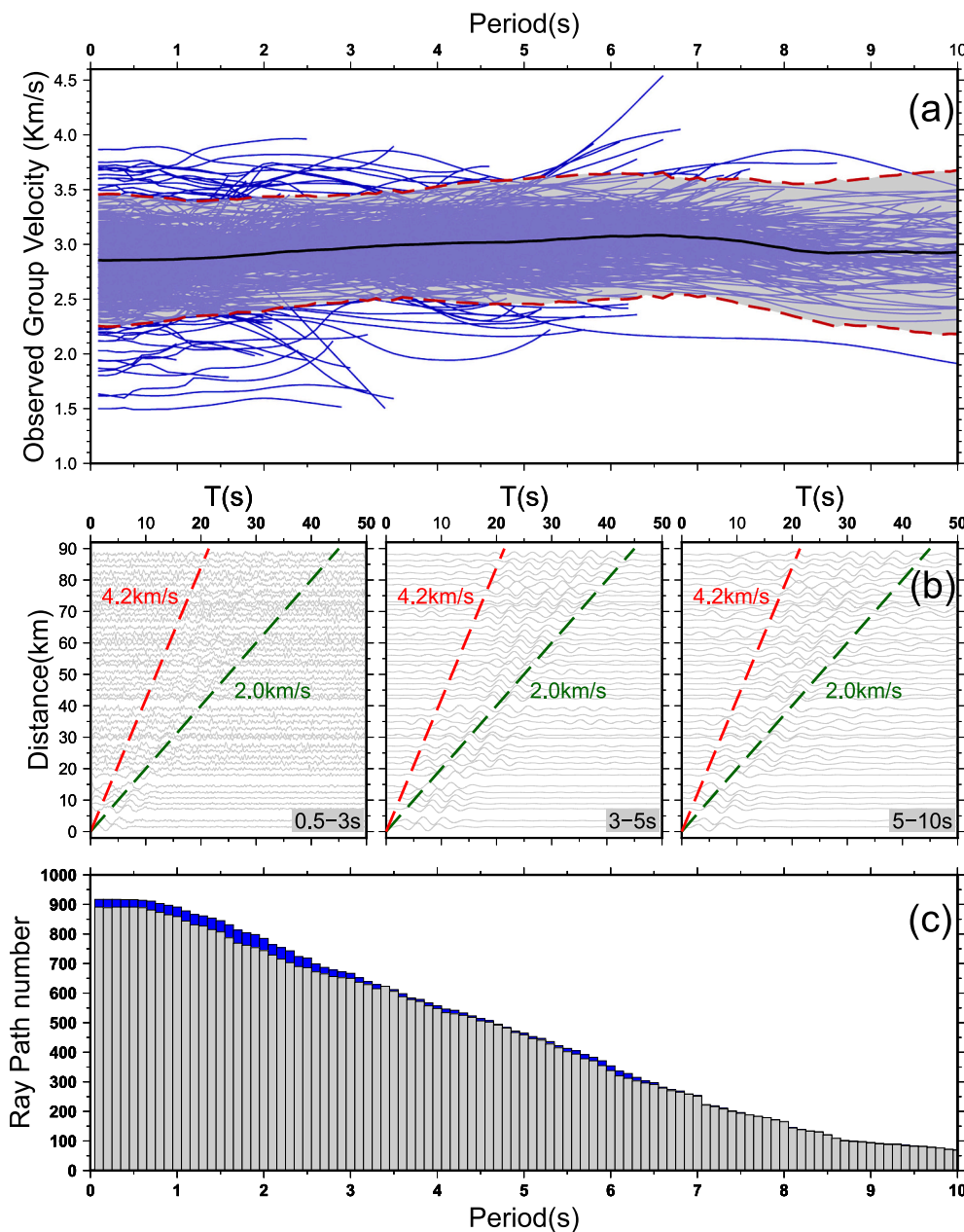
Fig. 3. (a) The blue lines show picked group velocity dispersion curves. The black dashed line is the average group velocity. Red dashed lines give the lower and upper boundaries of ±2.5 times the standard deviation. (b) Example of stacked NCFs (station JX22) at three different bandpass filters (0.1–3 s, 3–5 s, 5–10s) as a function of inter-station distance. (c) Number of ray path for each period. The blue histograms mark the dispersion removed by the "outlier removal". (For interpretation of the references to colour in this figure legend, the reader is referred to the web version of this article.)

dispersion between the reds dashed lines in Fig. 3a) range mostly between 2.5 km/s to 3.5 km/s, increasing gradually from the short period to the long period. Taking the station JX22 for example, the NCFs with other stations by using three different bandpass filters (0.5–3 s, 3–5 s, 5–10s) are shown in Fig. 3b. The NCFs reveals good dispersion feature of surface wave. Fig. 3c shows the number of ray paths at each period, which increase from ~100 to more than 900 from long period to short period. The total ray path number from 0.1 s to 10 s is 46,591, 45,252 after the "outlier removal". Detailed distribution of ray paths for each period is shown in Fig. S1.

In order to check the resolution along the depth, we calculate the sensitivity kernel of the group velocity on the S wave velocity at 0.1–10s period in Fig. 4. The reference S wave velocity was obtained by inverting the average group velocity dispersion (black dashed line in Fig. 3b). The sensitivity analysis shows the picked dispersion curves are sensitive to the S-wave velocity above 6 km.

We then did the checkerboard tests to analyze the horizontal resolution of group velocity maps with a banded model. Fig. 5 shows the

recovery of the checkerboard tests from 0.5 s to 4.5 s. When the anomalies are banded with 0.04°, the velocity structure can be recovered well near the areas covered by portable stations. As expected, the track covered by the portable stations has better recovery than other areas. More checkerboard tests at longer periods are shown in Fig. S2. According to the sensitivity kernel (Fig. 4) and checkerboard tests (Figs. 5, S2) for the observed dispersion data, the sensitivity coefficient is too small to target the velocity structure when the period is longer than 6 s and the checkerboard tests also show a bad recovery near Dahutang deposit after 6 s, therefore, we performed tomography by using dispersion data in the period of 0.1 to 5 s to guarantee the reliability.

5.2. Group velocity tomography

In this study, we obtained the Rayleigh wave group velocities at periods of 0.1–5 s by using a fast-marching algorithm (Rawlinson and Sambridge, 2005). Fig. 6 shows the distribution of group velocities at the period from 0.5 s to 4.5 s. The velocity variations are consistent with the
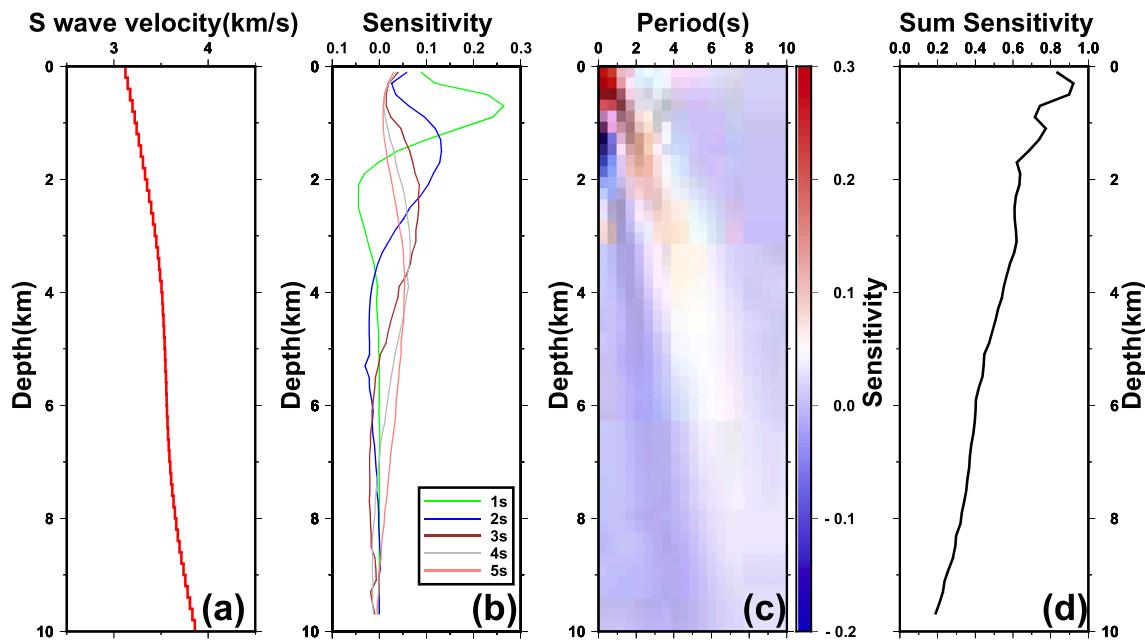
Fig. 4. Sensitivity analysis along the depth. (a) S-wave velocities inverted from average group velocity dispersion shown in Fig. 3(a). (b) Depth sensitivity kernel of the Rayleigh-wave group-velocities on the S-wave velocity for selected periods of 1, 2, 3, 4 and 5 s. (c) Depth sensitivity kernels at all periods (0.1–10 s). (d) The summation of the sensitivity in all periods.

shallow geological units at short periods. A high-velocity anomaly can be seen in the middle part of our array, corresponding to the shallow crystalline basement, while a low-velocity anomaly on both sides. Most of the faults (e.g. TWF, Tonggu-Wuning fault; JJF, Jiujiang-Jinan fault; YJF, Yifeng-Jingdezhen fault) appear in the low group velocity zones, especially when the period smaller than 3 s. It should be noted that we didn't interpret the high velocity in the south part at high frequency, regarding to the low resolution.

5.3. Moho depth and Vp/Vs

The stacked P receiver functions along the array show a clear Ps phase around 4 s, especially when summing them directly (SUM RF in Fig. 7b). In order to validate the quality of individual stations of H-κ stacking, we present the raw receiver functions and their H-κ stacking beneath six stations in Fig. S3. Three types of stacking, including Good, Not Bad, Bad, are marked. The quality of H–κ stacking result along the array are plotted with different colour, which is Not Bad in quality beneath our target region. The result shows an average Moho depth of 33.58 km (red dashed line in Fig. 8a). The Moho depth along the array deepens from south to north. Besides, the Vp/Vs values are generally below 1.75 along the array. However, the Vp/Vs ratios beneath Dahutang deposit (marked with circle) are slightly higher than that in the south and in the north (see Fig. 8b).

5.4. Shallow S-wave velocity structure from group wave dispersion

The shallow S-wave velocity structure inverted from dispersion by using CPS330 is shown in Fig. 9. In general, the velocity is low at both sides of the array and high in the middle. Right below the Dahutang deposit, there is a low velocity zone, which may be related to the mineralization process. We will discuss it in the following section.

5.5. Crustal S-wave velocity from joint inversion

For each station, we get 200,200 fitting models from the joint inversion. One example of the joint inversion at station JX02 (right blow the Dahutang deposit) is shown in Fig. 10, where the gray lines in the left

panel represent the best 2000 models, the blue line is the best-fitting model from dispersion inversion alone and the red line is the best-fitting model from joint inversion. The other two examples are shown in Fig. S4. The Vs model could recover well the observed Ps phase from the stacked receiver function and group velocity dispersion (right panel in Fig. 10). Due to the few teleseismic events during the deployed time (Table S1), the stacked receiver function may have large uncertainty. Hence we only invert Ps phase from receiver function to constrain the Moho depth. The velocity model from dispersion inversion alone (Fig. 11b) has a similar velocity pattern in the crust with that from joint inversion (Fig. 11a), making the results be convincing. In this study, we inverted the S-wave velocity structure down to 50 km (Fig. 11a), providing the possible deep information for the genesis mechanism of the deposit. Inside the region of Dahutang deposit, a high-velocity zone can be tracked from the lower crust (~25 km) up to 10 km. This is consistent with the results from ambient tomography at a large-scale region (Luo et al., 2019). At the top of the high velocity zone, there is a low-velocity zone with the depth shallower than 5 km that is consistent with the ambient noise tomography with the short period dispersion (Fig. 9). These low-velocity anomalies correspond to the large negative gravity anomalies (red arrows in Fig. 11a). Yao et al. (2013b) suggested that the negative gravity anomalies in Dahutang deposit resulted from the intrusion of the late Mesozoic granite, whose density is 0.09 g/cm3 lower than that of the surrounding rocks (the Neoproterozoic Jiuling granite). In order to analyze the possible origin of this gravity anomaly, we perform gravity modeling tests by setting the low-density body (20 km wide and 10 km thick, density anomaly = −0.09 g/cm3) at different depths (Fig. S5). The modeled gravity anomalies decrease if increasing the depth of the low-density body (Case A, B, and C in Fig. S5). Even if the low-density body at 30 km is set to 15 km thick (Case D), the generated gravity anomaly is too weak to match the observation. These tests indicate the negative anomalies origin from the shallow depth, and the resulted low-density body and the low-velocity zone from inversion are comparable. The Moho depth from H–κ stacking (red dots with white line) is in good agreement with the 4.2 km/s contour, confirming the reliability of our estimations.
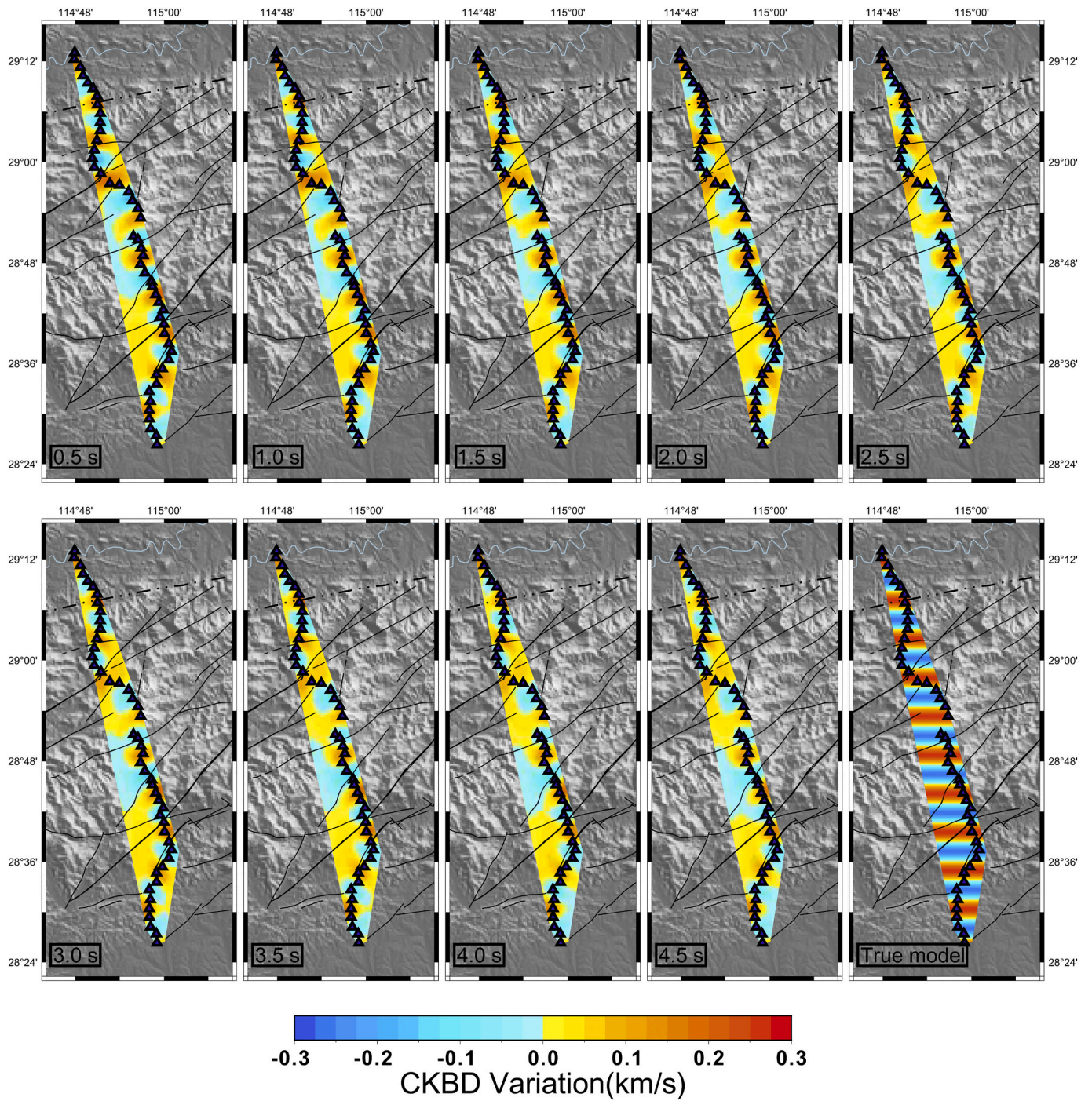
Fig. 5. Checkerboard tests for group velocity tomography with perturbation of ±0.3 km/s. The true model banded with 0.04° in all periods is shown in the right bottom of this panel. The blue triangles with black line show the deployed dense array. The black lines indicate the faults and geological boundary, the same as Fig. 1 (b). (For interpretation of the references to colour in this figure legend, the reader is referred to the web version of this article.)
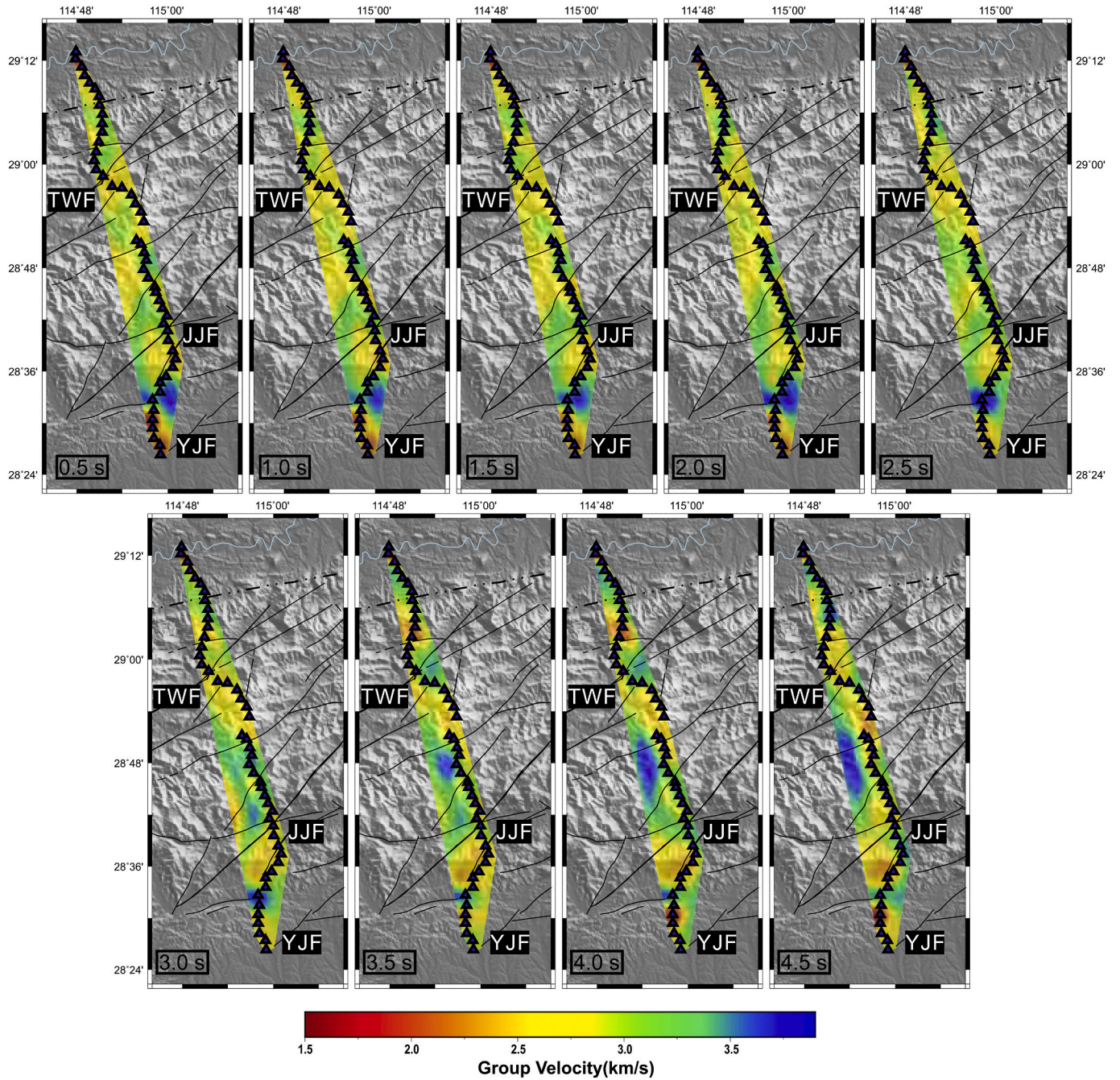
Fig. 6. Period-dependent group velocity maps at 0.5 s, 1.0, 1.5, 2.0, 2.5, 3.0, 3.5, 4.0 and 4.5 s. The blue triangles with black line show the deployed dense array. The black lines indicate the faults and geological boundary, the same as Fig. 1(b). Abbreviations: TWF, Tonggu-Wuning fault; JJF, Jiujiang-Jinan fault; YJF, Yifeng-Jingdezhen fault. (For interpretation of the references to colour in this figure legend, the reader is referred to the web version of this article.)
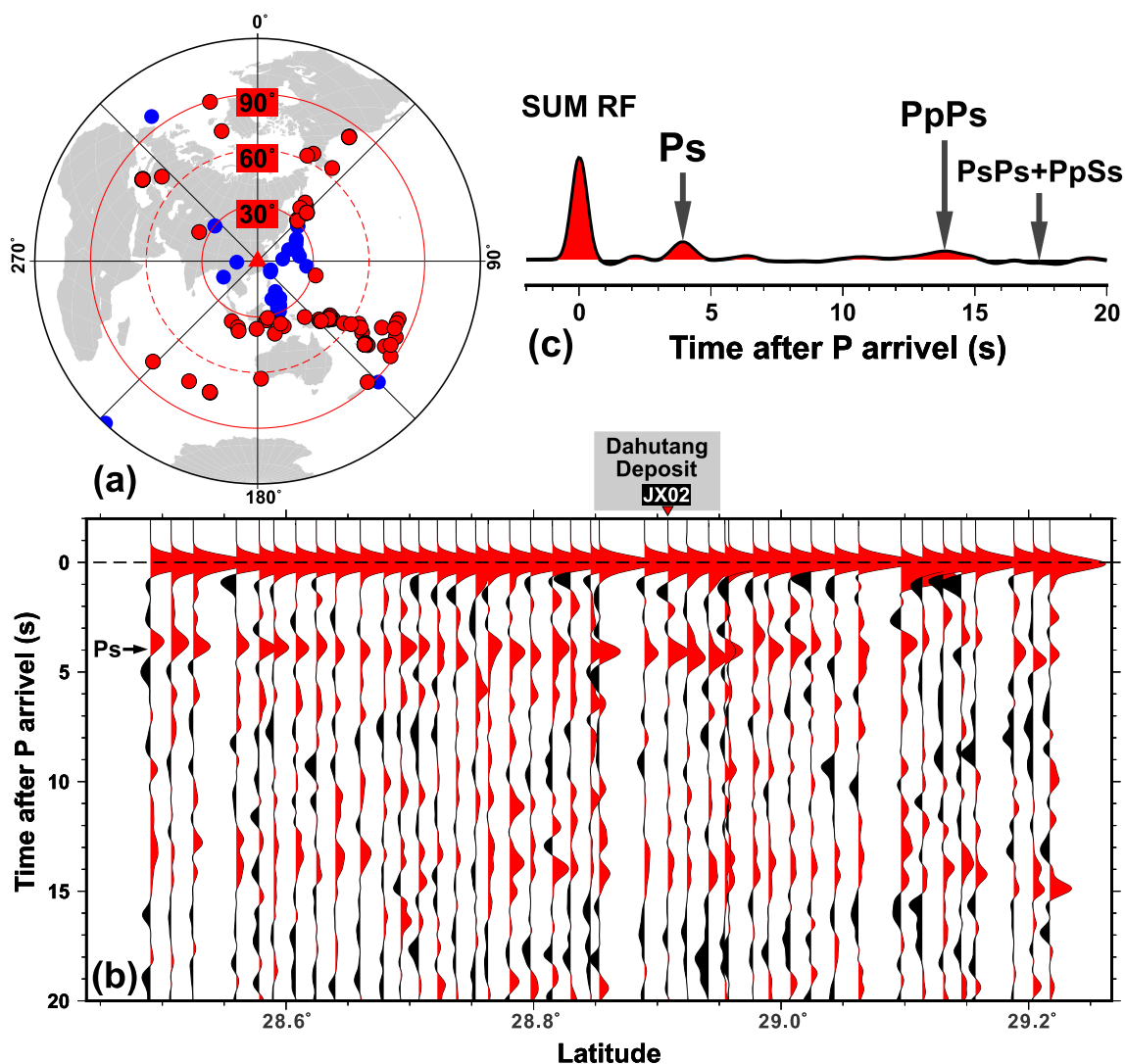
Fig. 7. (a) The distribution of teleseismic events used in this study. The red triangle marks the center of the study region. The red dots indicate the events we used to calculate PRFs. (b) P wave receiver functions along the station array. JX02 is marked for Fig. 10. (c) The summed receiver function (SUM RF). The Ps, PpPs, and PsPs+PpSs phase are marked with black arrows. (For interpretation of the references to colour in this figure legend, the reader is referred to the web version of this article.)

6. Discussion

According to the results from H-κ stacking (Fig. 8a) and joint inversion (Fig. 11a), the crustal thickness along the array ranges from 30.1 to 36.5 km. In general, the Moho depth gradually deepens along our array from south to north, where the south belongs to the Jiangnan orogen and the north belongs to the Yangtze block. This result is consistent with the large-scale Moho depth obtained by active seismic profiles (Deng et al., 2011), ambient noise tomography (Zhou et al., 2012; Shen et al., 2016) and joint inversion (Guo et al., 2019), as well as the thinner lithospheric thickness from Yangtze block to the coast obtained by S-wave receiver function (Li et al., 2013; Zhang et al., 2018a; Shen et al., 2019), and joint inversion of gravity and topography (Deng and Levandowski, 2018). Consequently, this result supports the Dahutang deposit is under the geodynamic setting of lithospheric thinning and extension due to the Paleo-Pacific plate subduction in the Late Mesozoic, the largest Phanerozoic tectonic-thermal events in South China (Wang et al., 2013).

The average Vp/Vs ratio of the crust ranges from 1.61 to 1.79, with an average value of 1.69. The values are comparable with 1.57–1.70 below the whole Jiangnan Orogen and Cathaysia block (Song et al., 2017) and 1.65–1.75 from Jiujiang to Nanning estimated by Zhao et al. (2015), even the uncertainties of our results are higher than 0.1 in some locations due to few receiver functions. It should be noted the Vp/Vs ratios are slightly higher beneath the deposit area (marked by the circle in Fig. 8) than that in the south and in the north. The higher Vp/Vs ratios imply that there are some mantle materials intruding in this region and engaging the mineralization. Nonetheless, the volume is not extensive as the very high velocity is not identified in the lower crust, which is consistent with our previous observation in the Cathaysia block (Deng et al., 2019a). The characteristics of Re—Os and Rb—Sr isotopes, and mineral paragenesis (Chen et al., 2018; Mao et al., 2011; Xiang et al., 2013a, 2013b; Zhang et al., 2016) also support involving of some mantle materials during the mineralization at Dahutang.
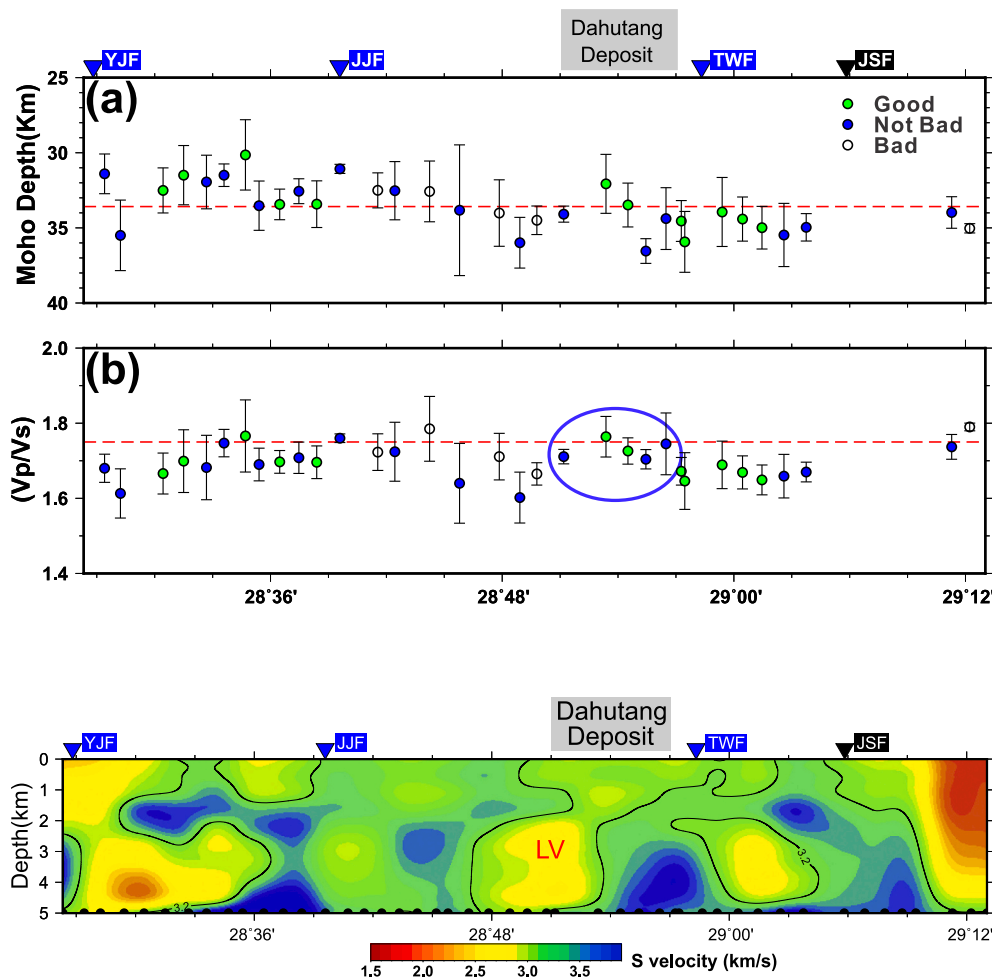
Fig. 8. Estimated Moho depths (a) and crustal Vp/Vs ratios (b) along the array. The error bars of Moho depths and Vp/Vs ratios are also plotted. The Vp/Vs ratios beneath Dahutang deposit are highlighted with a circle. Red dash line in (a) indicates the average Moho depth. Red dash line in (b) represents the Vp/Vs ratio of 1.75. Abbreviations: JSF, Jiujiang-Shitai fault; TWF, Tonggu-Wuning fault; JJF, Jiujiang-Jinan fault; YJF, Yifeng-Jingdezhen fault. The results are separated into 3 types of quality: Good in red colour, Not Bad in blue colour and Bad in white colour. (For interpretation of the references to colour in this figure legend, the reader is referred to the web version of this article.)

Fig. 9. Shallow S-wave velocity structure beneath the track of the array from ambient noise tomography. The blue triangles illustrate faults and black triangle marks the geological boundary. The dots in the bottom indicate the inversion points. Abbreviations: LV, Low-velocity zone; JSF, Jiujiang-Shitai fault; TWF, Tonggu-Wuning fault; JJF, Jiujiang-Jinan fault; YJF, Yifeng-Jingdezhen fault. (For interpretation of the references to colour in this figure legend, the reader is referred to the web version of this article.)

Compared with other seismic images beneath ore deposits, the low velocity in the upper crust seems a common feature, such as the low velocity from the dense ambient noise tomography at Karatungk Cu—Ni Mine in Xinjiang (Du et al., 2020), Baiyun Gold deposit in Liaoning (Li et al., 2020), ambient noise tomography at porphyry Cu deposit in southern Tibet (Huang et al., 2020), a dense active seismic image in Middle-Lower Yangtze metallogenic belt (Xu et al., 2014). Furtherly, combined with the result from joint inversion, we identify the high velocity zone beneath the low velocity zone that may indicate the possible differentiation of mineralization. We should note that this statement needs more dense seismic investigations and deep structure images in other ore deposits.

Based on the velocity feature, Moho depth and gravity anomaly, we propose a possible geological process for the formation of the Dahutang W—Cu deposit (Fig. 11b). Due to the extension and thinning of lithosphere during the Late Mesozoic in South China, the heat source from the upper mantle caused the lower crust partially melted. The hot melts then migrated from the lower crust to the middle and upper crust. After the crystallization and differentiation process, the denser material underwent a cooling process in the middle-lower crust to form the high S-wave velocity zones as shown in Fig. 11a. The lighter Si-rich components continue to migrate upward to form low-velocity granite which intruded into the Neoproterozoic Jiuling granite along faults. As the Neoproterozoic Jiuling granite already contained polymetallic components

such as tungsten (Jiang et al., 2015; Xiang et al., 2013a, 2013b), the intrusion of the late Mesozoic granite supplied the heat and material source for the further enrichment of tungsten ore. The differentiation process is consistent with the observation of highly differentiated granite at Dahutang region (Chen et al., 2018). The faults and extensional setting provide a necessary condition for the mineralization.

7. Conclusion

In order to image the deep structure beneath Dahutang Deposit, we deployed a dense seismic array and then applied ambient noise tomography, receiver function analysis and a joint inversion method to determine a high-resolution S-wave velocity structure. There are three main features: 1) The gravity anomaly is low at Dahutang deposit, and right below the deposit there is a low-velocity zone in the upper crust and high-velocity zone in the middle-lower crust; 2) Moho depth deepens from south to north along the array; 3) The Vp/Vs ratios are slightly higher beneath Dahutang deposit than that in the south and in the north.

Taking the advantage of the high resolution seismic image, our results support that this region is under the setting of lithosphere extension and thinning in the last tectonic-thermal event. This process provided a heat source for the melting of the lower crust, and the magma migrated upward and differentiated. The denser component cooled in the middle-
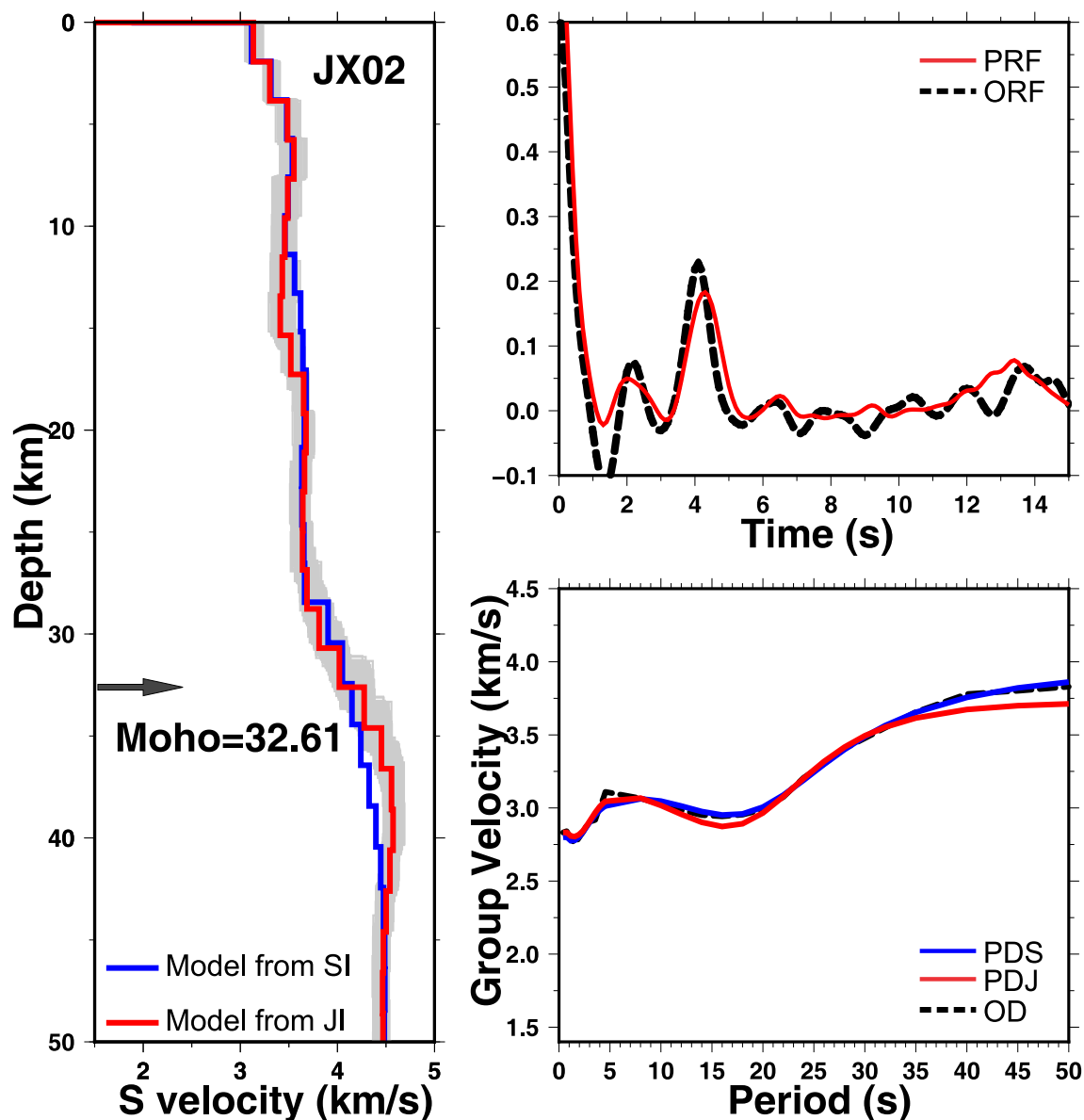
Fig. 10. Example of the joint inversion of receiver function and dispersion using observed data at station JX02 (the location is marked in Fig. 7(b)). The left panel: the best-fitting model of the dispersion inversion alone (blue line), the best-fitting model of the joint inversion (red line) and the best 2000 models (gray lines). The arrow marks the Moho depth from the joint inversion. The right top panel: the observed receiver function (ORF, black dashed line) and the predicated receiver function (PRF, red solid line) from the best-fitting model of the joint inversion; the right bottom panel: the observed Rayleigh wave group dispersion curve (ODS, black dashed line), the predicated Rayleigh wave group dispersion curve from surface wave dispersion (PDS, blue solid line), the predicated Rayleigh wave group dispersion curve from joint inversion (PDJ, red solid line). (For interpretation of the references to colour in this figure legend, the reader is referred to the web version of this article.)

lower crust to form the high velocity zones. The lighter component intruded into the Neoproterozoic granite in the late Mesozoic, which promoted the enrichment process of tungsten-copper polymetallic ore in Dahutang.

Data availability

The raw data could be downloaded from doi:10.6084/m9.fig-share.12609362.v1.

CRediT authorship contribution statement

Zhou Zhang: Investigation, Data curation, Visualization, Writing - original draft. **Yangfan Deng:** Project administration, Investigation, Data curation, Funding acquisition, Writing - review & editing. **Junming Yao:** Investigation, Writing - review & editing. Jianye Zong Investigation. **Huayong Chen:** Writing - review &

Declaration of Competing Interest

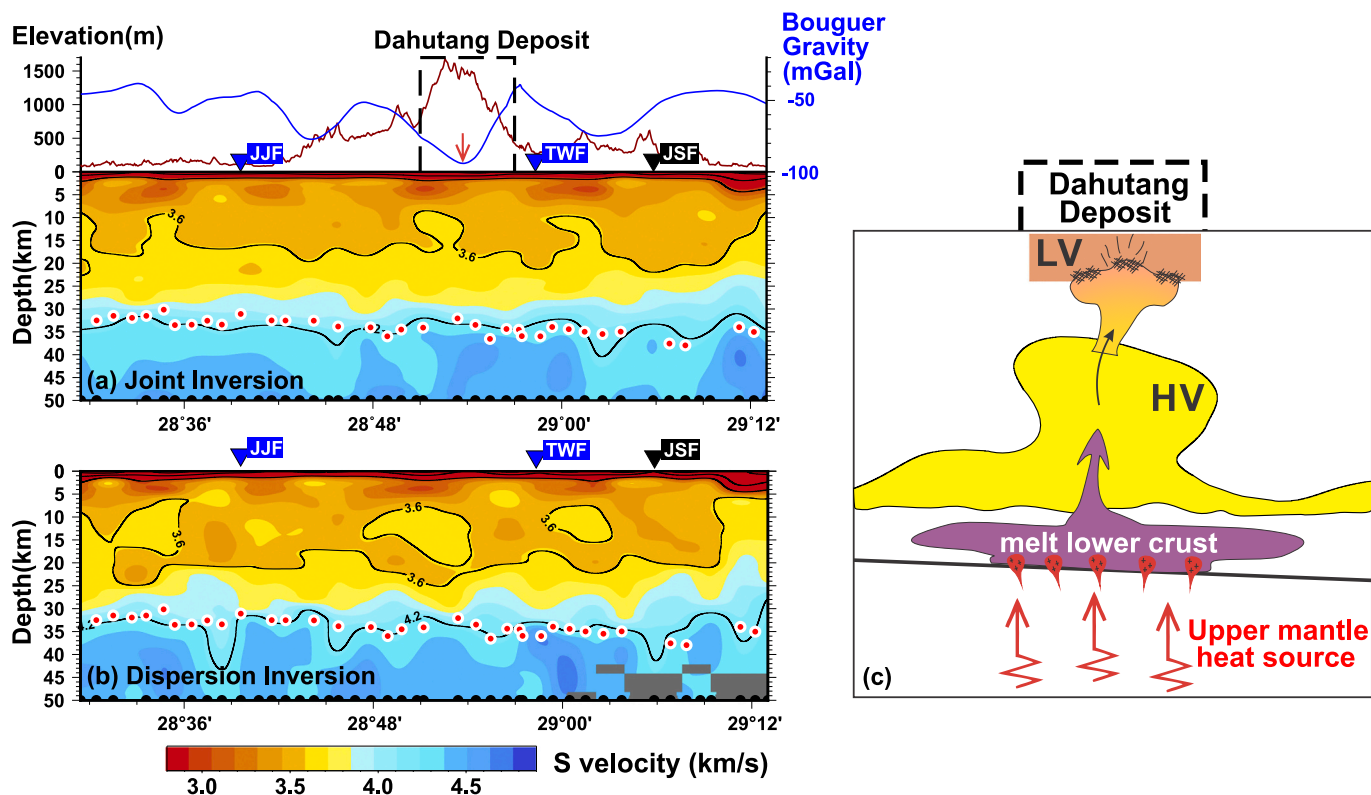The authors declare that they have no known competing financial

Fig. 11. (a) S-wave velocity along the array from joint inversion and (b) dispersion inversion alone. The topography (brown line) and the Bouguer Gravity anomaly (blue line) are shown in the top panel. The dots in the bottom indicate the inversion points. The red arrow at the top indicates the large largenegative gravity anomaly. The blue triangles mark the faults (JJF and TWF). Black triangle marks the geological boundary (JSF). The red dots with white line indicate the crustal thickness from H–κ stacking. (c) An schematic diagram for the mineralization processes of the Dahutang deposit. The black arrows indicate the migration of melt magma. The lithosphere extension and thinning process in the late Mesozoic provided a heat source for the melting of the lower crust, and the magma migrated upward and differentiated. The dense component cooled in the middle-lower crust to form the high velocity zones. The light component intruded into the Neo-proterozoic granite in the late Mesozoic, providing the heat and material source for the enrichment process of tungsten-copper polymetallic ore in Dahutang area. Abbreviations: JSF, Jiujiang-Shitai fault; TWF, Tonggu-Wuning fault; JJF, Jiujiang-Jinan fault; LV, Low-velocity zone; HV, High-velocity zone. (For interpretation of the references to colour in this figure legend, the reader is referred to the web version of this article.)

interests or personal relationships that could have appeared to influence the work reported in this paper.

Appendix A. Supplementary data

Supplementary table and figures to this article can be found online at https://doi.org/10.1016/j.pepi.2020.106617.

References

Bem, T.S., Yao, H., Luo, S., Yang, Y., Wang, X., Wang, X., Li, L., Liu, B., 2020. High-resolution 3-D crustal shear-wave velocity model reveals structural and seismicity segmentation of the central-southern Tanlu fault zone, eastern China. Tectonophysics 778, 228372. https://doi.org/10.1016/j.tecto.2020.228372.

Bensen, G.D., Ritzwoller, M.H., Barmin, M.P., Levshin, A.L., Lin, F., Moschetti, M.P., Shapiro, N.M., Yang, Y., 2007. Processing seismic ambient noise data to obtain reliable broad-band surface wave dispersion measurements. Geophys. J. Int. 169 (3), 1239–1260. https://doi.org/10.1111/j.1365-246X.2007.03374.x.

Cao, J., Yang, X., Zhang, D., Yan, F., 2020. In situ trace elements and Sr isotopes in scheelite and S-Pb isotopes in sulfides from the Shiweidong W–cu deposit, giant Dahutang ore field: implications to the fluid evolution and ore genesis. Ore Geol. Rev. 125, 103696. https://doi.org/10.1016/j.oregeorev.2020.103696.

Chen, W., Chen, B., Sun, K.K., 2018. Petrogenesis of the Maogongdong highly differentiated granite in the Dahutang tungsten ore field, Jiangxi Province. Acta Petrologica Sinica (in Chinese with English abstract) 34 (6), 1704–1724.

Chu, P.L., Duan, Z., Liao, S.B., Huang, W.C., Hong, W.T., Zhu, Y.H., Shu, X.J., 2019. Petrogenesis and tectonic significances of Late Mesozoic granitoids in the Dahutang area, Jiangxi Province: constraints from zircon U- Pb dating, mineral- chemistry, geochemistry and Hf isotope. Acta Geologica Sinica (in Chinese with English abstract) 93 (7), 1687–1707 doi:j.cnki.dizhixuebao.2019053.

Deng, Y., Levandowski, W., 2018. Lithospheric alteration, intraplate crustal deformation, and topography in eastern China. Tectonics 37 (11), 4120–4134. https://doi.org/10.1029/2018TC005079.

Deng, Q.D., Zhang, P.Z., Ran, Y.K., Yang, X.P., Min, W., Chen, L.C., 2003. Active tectonics and earthquake activities in China. Earth Sci. Front. (in Chinese with English abstract) 10 (S1), 66–73. https://doi.org/10.3321/j.issn1005-2321.2003.z1.012.

Deng, Y.F., Li, S.L., Fan, W.M., 2011. Crustal structure beneath South China revealed by deep seismic soundings and its dynamics implications. Chin J. Geophys. (in Chinese with English abstract) 2560–2574. https://doi.org/10.3969/j.issn.0001-5733.2011.10.013.

Deng, Y., Shen, W., Xu, T., Ritzwoller, M.H., 2015. Crustal layering in northeastern Tibet: a case study based on joint inversion of receiver functions and surface wave dispersion. Geophys. J. Int. 203 (1), 692–706. https://doi.org/10.1093/gji/ggv321.

Deng, Y., Zhang, Z., Badal, J., Fan, W., 2014. 3-D density structure under South China constrained by seismic velocity and gravity data. Tectonophysics 627, 159–170. https://doi.org/10.1016/j.tecto.2013.07.032.

Deng, Y.F., Li, J., Song, X., Zhu, L., 2018. Joint inversion for lithospheric structures: implications for the growth and deformation in northeastern Tibetan plateau. Geophys. Res. Lett. 45 (9), 3951–3958. https://doi.org/10.1029/2018GL077486.

Deng, Y., Li, J., Peng, T., Ma, Q., Song, X., Sun, X., Shen, Y., Fan, W., 2019a. Lithospheric structure in the Cathaysia block (South China) and its implication for the late Mesozoic magmatism. Phys. Earth Planet. Inter. 291, 24–34. https://doi.org/10.1016/j.pepi.2019.04.003.

Deng, Y.F., Li, J., Song, X., Li, H., Xu, T., 2019b. The lithospheric-scale deformation in NE Tibet from joint inversion of receiver function and surface wave dispersion. Terr. Atmos. Ocean. Sci. 30 (1), 127–137. https://doi.org/10.3319/TAO.2019.01.18.03.

Du, P., Wu, J., Li, Y., Wang, J., Han, C., Lindsay, M.D., Yuan, H., Zhao, L., Xiao, W., 2020. Imaging Karatungk Cu-Ni Mine in Xinjiang, Western China with a Passive Seismic Array. Minerals 2020 (10), 601. https://doi.org/10.3390/min10070601.

Feng, C.Y., Zhang, D.Q., Xiang, X.K., Li, D.X., Qu, H.Y., Liu, J.N., Xiao, Y., 2012. Re-Os isotopic dating of molybdenite from the Dahutang tungsten deposit in northwestern Jiangxi Province and its geological implication. Acta Petrologica Sinica (in Chinese with English abstract) 28 (12), 3858–3868.

Guo, L., Gao, R., Shi, L., Huang, Z., Ma, Y., 2019. Crustal thickness and Poisson's ratios of South China revealed from joint inversion of receiver function and gravity data. Earth Planet. Sci. Lett. 510, 142–152. https://doi.org/10.1016/j.epsl.2018.12.039.

Han, L., Huang, X., Li, J., He, P., Yao, J., 2016. Oxygen fugacity variation recorded in apatite of the granite in the Dahutang tungsten deposit, Jiangxi Province, South China. Acta Petrologica Sinica (in Chinese with English abstract) 32 (3), 746–758.

He, C.S., Dong, S.W., Santosh, M., Chen, X.H., 2013. Seismic evidence for a geosuture between the Yangtze and Cathaysia blocks, South China. Sci. Rep. 3, 2200. https://doi.org/10.1038/srep02200.

Herrmann, R.B., 2013. Computer programs in seismology: an evolving tool for instruction and research. Seismol. Res. Lett. 84 (6), 1081–1088. https://doi.org/10.1785/0220110096.

Hua, R., Chen, P., Zhang, W., Liu, X., Lu, J., Lin, J., Yao, J., Qi, H., Zhang, Z., Gu, S., 2003. Metallogenic systems related to Mesozoic and Cenozoic granitoids in South China. Sci. China Ser. D Earth Sci. 46 (8), 816–829. https://doi.org/10.1007/bf02879525.

Huang, L.C., Jiang, S.Y., 2012. Zircon U-Pb geochronology, geochemistry and petrogenesis of the porphyry-like muscovite granite in the Dahutang tungsten deposit, Jiangxi Province. Acta Petrologica Sinica (in Chinese with English abstract) 28, 3887–3900.

Huang, L.C., Jiang, S.Y., 2013. Geochronology, geochemistry and petrogenesis of the tungsten-bearing porphyritic granite in the Dahutang tungsten deposit, Jiangxi Province. Acta Petrologica Sinica (in Chinese with English abstract) 28, 4323–4335.

Huang, L.C., Jiang, S.Y., 2014. Highly-fractionated S-type granites from the giant Dahutang tungsten deposit in Jiangnan Orogen, Southeast China: geochronology, petrogenesis and their relationship with W mineralization. Lithos. 202–203, 207–226. https://doi.org/10.1016/j.lithos.2014.05.030.

Huang, S., Yao, H., Lu, Z., Tian, X., Zheng, Y., Wang, R., et al., 2020. High-resolution 3-D shear-wave velocity model of the Tibetan Plateau: implications for crustal deformation and porphyry Cu deposit formation. J. Geophys. Res. Solid Earth 125. https://doi.org/10.1029/2019JB019215 e2019JB019215.

Jiang, S.Y., Peng, N.J., Huang, L.C., Xu, Y.M., Zhan, G.L., Dan, X.H., 2015. Geological characteristic and ore genesis of the giant tungsten deposits from the Dahutang ore-concentrated district in northern Jiangxi Province. Acta Petrologica Sinica (in Chinese with English abstract) 31 (3), 639–655.

Kennett, B.L.N., Engdahl, E.R., 1991. Traveltimes for global earthquake location and phase identification. Geophys. J. Int. 105 (2), 429–465. https://doi.org/10.1111/j.1365-246X.1991.tb06724.x.

Li, X.H., Li, Z.X., Ge, W.C., Zhou, H.W., Li, W.X., Liu, Y., 2001. U–Pb zircon ages of the Neoproterozoic granitoids in South China and their tectonic implications. Bull. Mineral. Petrol. Geochem. (in Chinese with English abstract) 20 (4), 271–273.

Li, X.H., Li, Z.X., Ge, W., Zhou, H., Li, W., Liu, Y., Wingate, M.T., 2003. Neoproterozoic granitoids in South China: crustal melting above a mantle plume at ca. 825 Ma? Precambrian Res. 122 (1–4), 45–83. https://doi.org/10.1016/S0301-9268(02)00207-3.

Li, Q., Gao, R., Wu, F.T., Guan, Y., Ye, Z., Liu, Q., Hao, K.C., He, R., Li, W., Shen, X., 2013. Seismic structure in the southeastern China using teleseismic receiver functions. Tectonophysics 606, 24–35. https://doi.org/10.1016/j.tecto.2013.06.033.

Li, J., Dong, S., Zhang, Y., Zhao, G., Johnston, S.T., Cui, J., Xin, Y., 2016. New insights into Phanerozoic tectonics of South China: part 1, polyphase deformation in the Jiuling and Lianyunshan domains of the central Jiangnan Orogen. J. Geophys. Res. Solid Earth 121 (4), 3048–3080. https://doi.org/10.1002/2015jb012778.

Li, J., Song, X., Zhu, L., Deng, Y., 2017. Joint inversion of surface wave dispersions and receiver functions with P velocity constraints: application to southeastern Tibet. J. Geophys. Res. Solid Earth 122 (9), 7291–7310. https://doi.org/10.1002/2017JB014135.

Li, X.T., Huang, J.L., Liu, Z.K., 2020. Ambient-noise tomography of the Baiyun gold deposit in Liaoning, China. Seismol. Res. Lett. 91 (5), 2791–2802. https://doi.org/10.1785/0220190393.

Ligorría, J.P., Ammon, C.J., 1999. Iterative deconvolution and receiver-function estimation. Bull. Seismol. Soc. Am. 89 (5), 1395–1400.

Luo, S., Yao, H., Li, Q., Wang, W., Wan, K., Meng, Y., Liu, B., 2019. High-resolution 3D crustal S-wave velocity structure of the middle-lower Yangtze River Metallogenic Belt and implications for its deep geodynamic setting. Sci. China Earth Sci. 62, 1361–1378. https://doi.org/10.1007/s11430-018-9352-9.

Mao, J., Chen, M., Yuan, S., Guo, C., 2011. Characteristics and spatial-temporal regularity of mineral deposits in Qinhang (or Shihang) Metallogenic Belt, South China. Acta Geologica Sinica (in Chinese with English abstract) 85 (5), 636–658.

Mao, Z., Cheng, Y., Liu, J., Yuan, S., Wu, S., Xiang, X., Luo, X., 2013. Geology and molybdenite re–Os age of the Dahutang granite-related veinlets-disseminated tungsten ore field in the Jiangxin Province, China. Ore Geol. Rev. 53, 422–433. https://doi.org/10.1016/j.oregeorev.2013.02.005.

Mao, Z.H., Liu, J.J., Mao, J.W., Deng, J., Zhang, F., Meng, X.Y., Xiong, B.K., Xiang, X.K., Luo, X.H., 2015. Geochronology and geochemistry of granitoids related to the giant Dahutang tungsten deposit, middle Yangtze River region, China: implications for petrogenesis, geodynamic setting, and mineralization. Gondwana Res. 28, 816–836. https://doi.org/10.1016/j.gr.2014.07.005.

Pavlis, N.K., Holmes, S.A., Kenyon, S.C., Factor, J.K., 2012. The development and evaluation of the earth gravitational model 2008 (EGM2008). J. Geophys. Res. Solid Earth 117 (B4). https://doi.org/10.1029/2011JB008916.

Rawlinson, N., Sambridge, M., 2005. The fast marching method: an effective tool for tomographic imaging and tracking multiple phases in complex layered media. Explor. Geophys. 36 (4), 341–350. https://doi.org/10.1071/eg05341.

Rawlinson, N., Reading, A.M., Kennett, B.L., 2006. Lithospheric structure of Tasmania from a novel form of teleseismic tomography. J. Geophys. Res. Solid Earth 111 (B2). https://doi.org/10.1029/2005JB003803.

Shen, W., Ritzwoller, M.H., Kang, D., Kim, Y., Lin, F.C., Ning, J., Wang, W., Zheng, Y., Zhou, L., 2016. A seismic reference model for the crust and uppermost mantle beneath China from surface wave dispersion. Geophys. J. Int. 206 (2), 954–979. https://doi.org/10.1093/gji/ggw175.

Shen, X., Kind, R., Huang, Z., Yuan, X., Liu, M., 2019. Imaging the mantle lithosphere below the China cratons using S-to-p converted waves. Tectonophysics 754, 73–79. https://doi.org/10.1016/j.tecto.2019.02.002.

Shu, L.S., 2012. An analysis of principal features of tectonic evolution in South China block. Geol. Bull. China (in Chinese with English abstract) 31, 1035–1053. https://doi.org/10.1007/s11783-011-0280-z.

Song, P., Zhang, X., Liu, Y., Teng, J., 2017. Moho imaging based on receiver function analysis with teleseismic wavefield reconstruction: application to South China. Tectonophysics 718, 118–131. https://doi.org/10.1016/j.tecto.2017.05.031.

Song, W., Yao, J., Chen, H., Sun, W., Lai, C., Xiang, X., et al., 2018a. A 20 my long-lived successive mineralization in the giant Dahutang W–Cu–Mo deposit, South China. Ore Geol. Rev. 95, 401–407. https://doi.org/10.1016/j.oregeorev.2018.02.033.

Song, W.L., Yao, J.M., Chen, H.Y., Sun, W.D., Ding, J.Y., Xiang, X.K., et al., 2018b. Mineral paragenesis, fluid inclusions, H–O isotopes and ore-forming processes of the giant Dahutang W–Cu–Mo deposit, South China. Ore Geol. Rev. 99, 116–150. https://doi.org/10.1016/j.oregeorev.2018.06.002.

Sun, W.D., Yang, X.Y., Fan, W.M., Wu, F.Y., 2012. Mesozoic large scale magmatism and mineralization in South China: preface. Lithos 150, 1–5. https://doi.org/10.1016/j.lithos.2012.06.028.

Wang, Y., Fan, W., Zhang, G., Zhang, Y., 2013. Phanerozoic tectonics of the South China block: key observations and controversies. Gondwana Res. 23 (4), 1273–1305. https://doi.org/10.1016/j.gr.2012.02.019.

Wessel, P., Smith, W.H., Scharroo, R., Luis, J., Wobbe, F., 2013. Generic mapping tools: improved version released. EOS Trans. Am. Geophys. Union 94 (45), 409–410. https://doi.org/10.1002/2013EO450001.

Xiang, X.K., Chen, M.S., Zhan, G.N., Qian, Z.Y., Li, H., Xu, J.H., 2012. Metallogenic geological conditions of Shimensi tungsten-polymetallic deposit in North Jiangxi Province. Contr. Geol. Miner. Resour. Res. (in Chinese with English abstract) 27, 143–155. https://doi.org/10.6053/j.issn.1001-1412.2012.02.002.

Xiang, X.K., Wang, P., Sun, D.M., Zhong, B., 2013a. Re-Os isotopic age of molybdeinte from the Shimensi tungsten polymetallic deposit in northern Jiangxi Province and its geological implications. Geol. Bull. China (in Chinese with English abstract) 32 (11), 1824–1831. https://doi.org/10.3969/j.issn.1671-2552.2013.11.015.

Xiang, X.K., Wang, P., Sun, D.M., Zhong, B., 2013b. Isotopic geochemical characteristics of the Shimensi tungsten-polymetallic deposit in northern Jiangxi Province. Acta Geoscientica Sinica (in Chinese with English abstract) 34 (3), 263–271. https://doi.org/10.3975/cagsb.2013.03.02.

Xu, T., Zhang, Z.J., Tian, X.B., Liu, B.F., Bai, Z.M., Lü, Q.T., Teng, J.W., 2014. Crustal structure beneath the middle-lower Yangtze metallogenic belt and its surrounding areas:constraints from active source seismic experiment along the Lixin to Yixing profile in East China. Acta Petrol. Sin. 30 (4), 918–930 (in Chinese with English abstract).

Yang, X., Sun, W., 2018. Jurassic and cretaceous (Yanshannian) tectonics, magmatism and metallogenesis in South China: preface. Int. Geol. Rev. 60 (11–14), 1321–1325.

Yao, H.J., Van Der Hilst, R.D., De Hoop, M.V., 2006. Surface-wave array tomography in SE Tibet from ambient seismic noise and two-station analysis—I. phase velocity maps. Geophys. J. Int. 166 (2), 732–744. https://doi.org/10.1111/j.1365-246X.2006.03028.x.

Yao, J., Shu, L., Santosh, M., Li, J., 2013a. Geochronology and Hf isotope of detrital zircons from Precambrian sequences in the eastern Jiangnan Orogen: constraining the assembly of Yangtze and Cathaysia blocks in South China. J. Asian Earth Sci. 74, 225–243. https://doi.org/10.1016/j.jseaes.2012.08.010.

Yao, S.P., Ding, S.H., Huang, J.M., Jiang, J.J., Yan, J.L., 2013b. Metallogenic prediction of Dahutang W-Cu-Mo deposit based on the gravity anomaly. Conserv. Utiliz. Mineral Res. (03), 14–18. https://doi.org/10.3969/j.issn.1001-0076.2013.03.004 in Chinese with English abstract.

Yao, J., Mathur, R., Sun, W., Song, W., Chen, H., Mutti, L., Xiang, X., Luo, X., 2016. Fractionation of Cu and Mo isotopes caused by vapor-liquid partitioning, evidence from the Dahutang W-Cu-Mo ore field. Geochem. Geophys. Geosyst. 17 (5), 1725–1739. https://doi.org/10.1002/2016GC006328.

Ye, H.M., Zhang, X., Zhu, Y.H., 2016. In-situ monazite U-Pb geochronology of granites in Shimensi tungsten polymetallic deposit, Jiangxi Province and its geological significance. Geotectonica et Metallogenia (in Chinese with English abstract) 40 (1), 58–70.

Ye, Z., Li, J., Gao, R., Song, X., Li, Q., Li, Y., Xu, X., Huang, X., Xiong, X., Li, W., 2017. Crustal and uppermost mantle structure across the Tibet-Qinling transition zone in NE Tibet: implications for material extrusion beneath the Tibetan plateau. Geophys. Res. Lett. 44 (20), 10,316–310,323. https://doi.org/10.1002/2017GL075141.

Yuan, X., Ni, J., Kind, R., Mechie, J., Sandvol, E., 1997. Lithospheric and upper mantle structure of southern Tibet from a seismological passive source experiment. J. Geophys. Res. Solid Earth 102 (B12), 27491–27500. https://doi.org/10.1029/97JB02379.

Zhang, M.Y., Feng, C.Y., Li, D.X., Wang, H., Zhou, J.H., Ye, S.Z., Wang, G.H., 2016. Geochronological study of the Kunshan W-Mo-Cu deposit in the Dahutang area, northern Jiangxi Province and its geological significance. Geotecton. Metallog. 40 (3), 503–516. https://doi.org/10.16539/j.ddgzyckx.2016.03.008 in Chinese with English abstract.

Zhang, Y.Y., Chen, L., Ai, Y.S., Jiang, M.M., Xu, W.W., Shen, Z.Y., 2018a. Lithospheric structure of the South China block from S-receiver function. Chinese. J. Geophys. 61 (1), 138–149. https://doi.org/10.6038/cjg2018L0226 in Chinese with English abstract.

Zhang, Y., Gao, J.F., Ma, D., Pan, J., 2018b. The role of hydrothermal alteration in tungsten mineralization at the Dahutang tungsten deposit, South China. Ore Geol. Rev. 95, 1008–1027. https://doi.org/10.1016/j.oregeorev.2018.04.006.

Zhao, Y.N., Duan, Y.H., Zou, C.Q., Wei, Y.H., Qiu, Y., Lin, J.Y., Li, X.M., 2015. Study of the receiver function profile from Jiujiang, Jiangxi Province to Ninghua, Fujian Province. Acta Seismol. Sin. 37 (5), 722–732. https://doi.org/10.11939/jass.2015.05.002 in Chinese with English abstract.

Zhou, B.X., Sun, T., Shen, W., Shu, L., Niu, Y., 2006. Petrogenesis of Mesozoic granitoids and volcanic rocks in South China: a response to tectonic evolution. Episodes 29 (1), 26. https://doi.org/10.18814/epiiugs/2006/v29i1/004.

Zhou, L., Xie, J., Shen, W., Zheng, Y., Yang, Y., Shi, H., Ritzwoller, M.H., 2012. The structure of the crust and uppermost mantle beneath South China from ambient noise and earthquake tomography. Geophys. J. Int. 189 (3), 1565–1583. https://doi.org/10.1111/j.1365-246X.2012.05423.x.

Zhu, L., Kanamori, H., 2000. Moho depth variation in southern California from teleseismic receiver functions. J. Geophys. Res. Solid Earth 105 (B2), 2969–2980. https://doi.org/10.1029/1999JB900322.